

Mechanism of the CaIrO_3 post-perovskite phase transition under pressure

Penghao Xiao,¹ Jin-Guang Cheng,² Jian-Shi Zhou,² John B. Goodenough,² and Graeme Henkelman^{1,2,*}

¹*Department of Chemistry and the Institute for Computational and Engineering Sciences,
University of Texas at Austin, Austin, Texas 78712, USA*

²*Texas Materials Institute, University of Texas at Austin, Austin, Texas 78712, USA*

(Received 24 May 2013; published 8 October 2013)

Recent experiments have shown that the perovskite to post-perovskite phase transformation in CaIrO_3 occurs more readily at room temperature when a shear stress is applied as compared to isotropic pressure. To understand this mechanistically, we have calculated the minimum-energy pathway of the phase transition with density functional theory under different pressure conditions with the generalized solid-state nudged elastic band method. Our results reveal that shear stress significantly lowers the barrier and stabilizes the product state while isotropic pressure initially raises the barrier and only reduces the barrier at pressures above 90 GPa. The nonmonotonic change in barrier with isotropic pressure is explained in terms of an increase in the activation volume under low pressure and a decrease under high pressure.

DOI: 10.1103/PhysRevB.88.144102

PACS number(s): 64.70.kp

I. INTRODUCTION

Aided by laser-heating in a diamond-anvil cell, the principal constituent of the Earth's lower mantle, MgSiO_3 perovskite (Pv), was recently found to transform into a post-perovskite (pPv) structure above 125 GPa and 2500 K, which corresponds to the pressure and temperature conditions at the Earth's lowermost mantle, or D'' layer.¹⁻³ Following the discovery of pPv MgSiO_3 , a number of other ABO_3 perovskites, e.g., CaBO_3 ($B = \text{Ru, Rh, Sn, Ir}$) have been transformed into the pPv structure under high-pressure and/or high-temperature conditions.⁴⁻⁸ Unlike MgSiO_3 , the Ca-based pPv are stable at ambient conditions, which makes them excellent analog materials of MgSiO_3 .

Recently, high-pressure experiments on Pv CaIrO_3 demonstrate that the Pv to pPv transition can indeed be induced at room temperature at relatively low pressures in the presence of a significant shear stress^{9,10} whereas the Pv phase remains stable up to 31 GPa at room temperature under isotropic pressure conditions.¹¹

In order to understand the mechanism of the Pv-to-pPv transition under pressure, and especially in the presence of shear stress, it is important to determine the transition process at the atomic scale. In previous theoretical studies of MgSiO_3 , the Pv-to-pPv transition has been determined under extremely high-pressure conditions (≥ 120 GPa).^{3,12} It was found that the transition occurs through a shear or slide mechanism, which implies that shear stress should facilitate the Pv-to-pPv transition. However, the pressures and temperatures considered in the simulations were so high that the conclusions may not be extendable to room-temperature and lower pressure conditions. All applied stresses in these previous studies were taken to be isotropic and the role of pressure was primarily understood as stabilizing the pPv phase; how pressure affects the transition temperature and activation energy has not been investigated. Another concern about these previous studies is that the transition mechanisms were found only in the degrees of freedom used to define the periodic cell. This so-called rapid-nuclear-motion approximation¹³ can give incorrect barriers, or fail to find a true minimum-energy path if the reaction mechanism also involves motions of

the atoms within the cell.¹⁴ The focus of this work is thus to investigate the dynamics of the Pv-to-pPv transition in CaIrO_3 under different pressure and shear conditions by using the generalized solid-state nudged elastic band (G-SSNEB) method,¹⁴ which treats both cell and atomic degrees of freedom on an equal footing.

A common approximation, within the context of transition state theory, is that the most probable reaction pathway is the minimum-energy path (MEP) and the maximum energy along the path with respect to the initial state (the barrier) largely determines the rate of the reaction at a specified temperature. When the reaction pathway is determined, the influence of an external pressure on the barrier can also be calculated.¹⁵ Under constant pressure, the energy landscape $E(\mathbf{R})$ can be generalized to an enthalpy landscape $H(\mathbf{R})$,

$$H(\mathbf{R}) = E(\mathbf{R}) + PV(\mathbf{R}), \quad (1)$$

where \mathbf{R} represents the geometry configuration, P is the external pressure, and V is the volume of the system. The difference between the energy and enthalpy barrier is the $P\Delta V$ work done by the external pressure. For solid-state systems, the pressure can be anisotropic and should be expressed as a stress tensor. The work W done by the external pressure is then written in the general form

$$W = V \sum_{ij} \sigma_{ij}^{\text{ext}} \epsilon_{ij}, \quad (2)$$

where σ_{ij}^{ext} is the stress tensor and ϵ_{ij} is the strain tensor. In the low-pressure regime, the barrier change is primarily from the work term. When the pressure is high enough, the barrier geometry can also change, and this contribution to the activation enthalpy cannot be ignored.¹⁶

The main results in this paper are as follows. First, we investigate the atomic mechanism of the Pv-to-pPv phase transition by locating the MEP in the enthalpy landscapes with the G-SSNEB method.¹⁴ Our results directly show that shear stress decreases the barrier while the isotropic pressure increases the barrier at low pressure and only decreases the barrier when the pressure is over 90 GPa. This surprising behavior is a result of the reaction pathway being along

the shear deformation direction under all pressure conditions while the volume can either expand or shrink from the reactant to the saddle point depending on the isotropic pressure applied. We also find an interesting intermediate minimum between the two phases in which every other layer of iridium atoms are coordinated by four oxygen in a square-planar geometry. A nucleation-like layer by layer growth of the pPv phase is observed in a sufficiently large supercell.

II. METHOD

For solid-state systems described by periodic boundary conditions, the geometric configuration vector \mathbf{R} includes two types of variables: atomic positions \mathbf{r} , and cell vectors \mathbf{h} . To define distances in this generalized configuration space, a Jacobian (metric) is required to balance the two vectors. Our choice of Jacobian is made so that the ratio between distances is invariant to the supercell representation of the material. To satisfy this requirement, the distance between two points in configuration space is defined as

$$\|\Delta\mathbf{R}\| = \sqrt{NL^2\|\bar{\boldsymbol{\epsilon}}\|^2 + \|\Delta\mathbf{r}\|^2}, \quad (3)$$

which is the norm of the generalized configuration vector

$$\Delta\mathbf{R} = \{\sqrt{N}L\bar{\boldsymbol{\epsilon}}, \Delta\mathbf{r}\} \quad (4)$$

$$= \{J\bar{\boldsymbol{\epsilon}}, \Delta\mathbf{r}\}, \quad (5)$$

where $\bar{\boldsymbol{\epsilon}}$ is the average strain, $\Delta\mathbf{r}$ is the pure atomic motion in Cartesian coordinates, N is the number of atoms in the supercell, L is the average distance between atoms, and $J = \sqrt{N}L$ is the Jacobian, which has the unit of this length. Based on the general distance defined above, the corresponding general force is

$$\mathbf{F} = \left\{ \frac{\Omega}{J} (\boldsymbol{\sigma}^{\text{cauchy}} + \boldsymbol{\sigma}^{\text{ext}}), \mathbf{f} \right\}, \quad (6)$$

where Ω is the volume of the supercell; $\boldsymbol{\sigma}^{\text{cauchy}}$ and $\boldsymbol{\sigma}^{\text{ext}}$ are the Cauchy and the external stress, respectively; \mathbf{f} is the regular atomic force. It is then clear that

$$\mathbf{F} \cdot \Delta\mathbf{R} = \Delta E + \Omega\boldsymbol{\sigma}^{\text{ext}} \cdot \bar{\boldsymbol{\epsilon}} = \Delta H. \quad (7)$$

In this generalized coordination system, a structure optimization following the steepest decent direction is simply $\Delta\mathbf{R} = \alpha\mathbf{F}$. The nudged elastic band method implemented in the generalized coordination system is the G-SSNEB method.¹⁴

In our calculations, the forces and stresses are evaluated with density functional theory (DFT)¹⁷ in the general gradient approximation as implemented in the Vienna Ab Initio Simulation package.^{18,19} The Perdew-Wang functional is adopted for the exchange-correlation energy.²⁰ Core electrons are described by pseudopotentials generated from the projector augmented wave method,^{21,22} and valence electrons are expanded in a plane-wave basis set with an energy cutoff of 400 eV. A Hubbard model correction is applied to avoid overdelocalization of iridium 5d electrons due to self-repulsion. An effective U value of 2.8 eV is chosen to fit to the band gap of the pPv structure.²³ Unlike the electronic structure, the reaction pathway is not sensitive to small changes

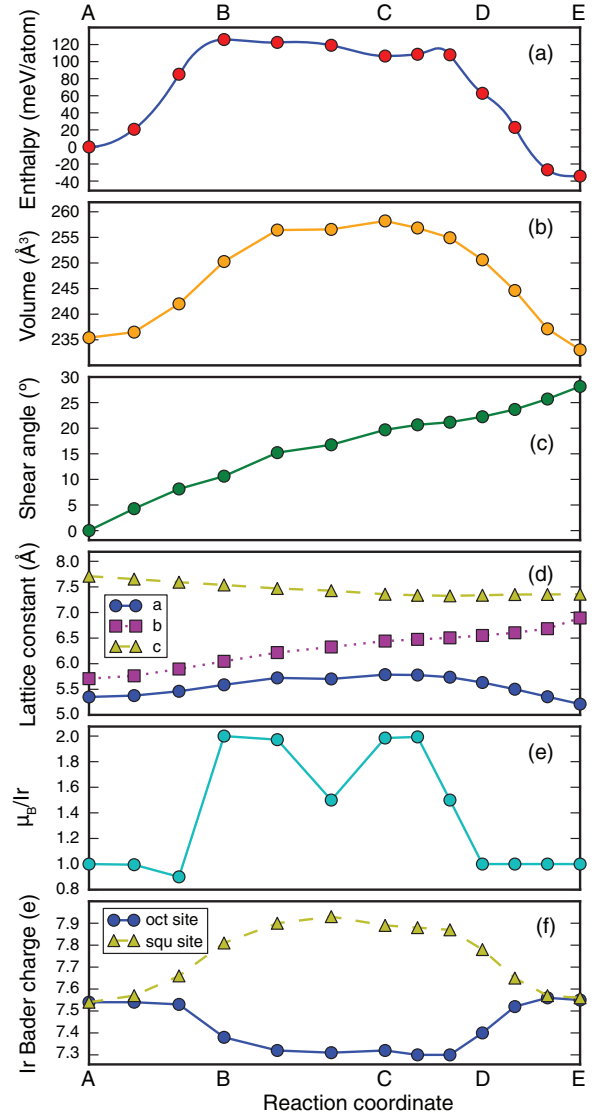


FIG. 1. (Color online) Properties of the minimum-energy phase transformation path at zero pressure. The reaction coordinate is the accumulated configurational change [Eq. (4)] along the path. In subsequent figures, the reaction coordinate is scaled between 0 and 1; here the letters indicate key structures along the path, shown in the next figure.

of the U value. For the same reason, spin-orbit coupling (SOC) is not considered in our calculations either.

A. Results

In contrast with the Pv structure, which has a three-dimensional network of corner-linked IrO_6 octahedra, the pPv structure consists of IrO_6 octahedral layers formed by both corner and edge sharing. The phase transition thus involves octahedral rotations and rearrangement. We started with the atom mapping reported in Refs. 3,10, and 12 as an initial path, and then calculated the MEP with zero external pressure using the G-SSNEB. The converged MEP, shown in Fig. 1(a), is a concerted mechanism with a barrier of 125 meV/atom. Structures along the MEP are shown in Fig. 2. Along the transition path, the iridium atom in the center of the cell breaks two Ir-O bonds and forms a square planar coordination, while

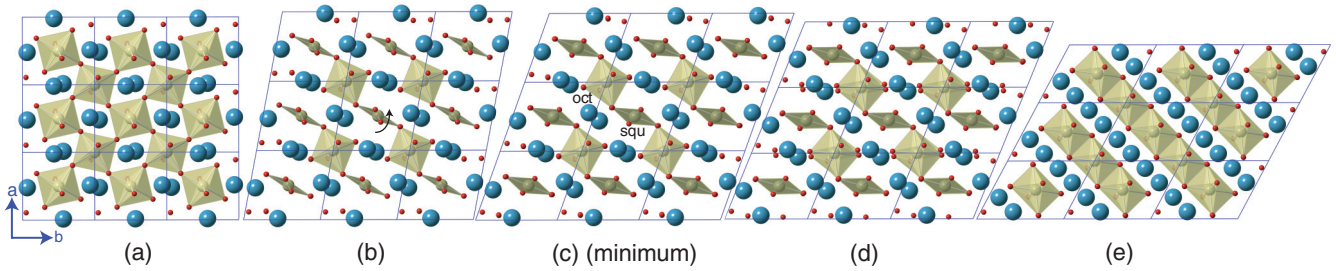


FIG. 2. (Color online) Structures along the minimum-energy phase transformation path at zero pressure. The polyhedra are IrO₆; the big blue circles are Ca; the small red circles are O.

its four neighboring IrO₆ remain intact. Meanwhile the center IrO₄ plane rotates slightly to align the Ir-O bond parallel to the neighbors as the arrow indicates in structure B. As the cell continues shearing, two neighboring IrO₆ groups move closer to the center iridium atom and rotate around the shared oxygen to form two new Ir-O bonds. Movies of the structural evolution can be found in the Supplemental Material.²⁴

The intermediate minimum along the path, labeled C in Fig. 2, is characterized with alternating connected square-planar and octahedral units. The intermediate minimum is so shallow that this structure might be difficult to stabilize in an experiment. A Bader analysis^{25,26} for the images in Fig. 1(f) shows that a charge transfer occurs between two types of iridium atoms; the iridium in octahedral sites lose electrons to the iridium in square-planar sites during the transition. This can be understood from crystal-field theory. Each iridium atom in the Pv phase originally has five *d* electrons in a low-spin configuration. As some sites become less coordinated, the elongation of the two oxygen bonds in the *z* direction lowers the energy of *d*_{yz}, *d*_{xz}, and *d*_{z²} orbitals. When the *d*_{z²} level of the square-planar site is close to or lower than the *t*_{2g} level of the octahedral site, one paired electron from the latter level transfers to the former one to maximize the multiplicity. The Bader charges are not integers, but translated to the conventional picture of discrete charge transfer, they indicate that the octahedral iridium now has four *d* electrons and the square-planar has six. This charge-transfer picture is consistent with the increase of the average spin magnetic moment of iridium in Fig. 1(e). Although the value of the spin moment is not precise in the absence of SOC, there is no doubt that the charge transfer results in a spin moment change, which should be observable in experiment.

The volume change and shear deformation angle are plotted as a function of the reaction coordinate in Figs. 1(b) and 1(c). The volume increases first and then decreases, while the shear angle increases monotonously. Bell's theory says that the enthalpy barrier height is a linear function of external force.^{16,27} In a first-order approximation, the positions of the saddle point and minima are not changed by the external force so that the enthalpy barrier change due to the external force is only determined by the work term. Extended to solid-state systems, Bell's theory says that in the low-pressure regime the barrier is a linear function of the stress tensor,

$$H^\ddagger(\boldsymbol{\sigma}^{\text{ext}}) - H^0(\boldsymbol{\sigma}^{\text{ext}}) = E^\ddagger(0) - E^0(0) - \Omega^0 \sum_{ij} \sigma_{ij}^{\text{ext}} \epsilon_{ij}^\ddagger(0), \quad (8)$$

where H^0 and H^\ddagger are the enthalpies of the reactant and transition state, respectively. $E^0(0)$ and $E^\ddagger(0)$ are the energies of the reactant and transition state under zero pressure. The last term is the work done by the external stress from the reactant to the transition state. The isotropic compression is against the reaction direction (volume expansion), thus increasing the barrier; the shear stress is along the reaction direction (shear deformation), thus decreasing the barrier. In the high-pressure regime, shifts of the critical points are significant so that new G-SSNEB calculations with the external stresses applied are required.

A set of MEPs and barriers from G-SSNEB calculations at different external compression conditions are plotted in Fig. 3. As expected from Eq. (8), the shear stress lowers

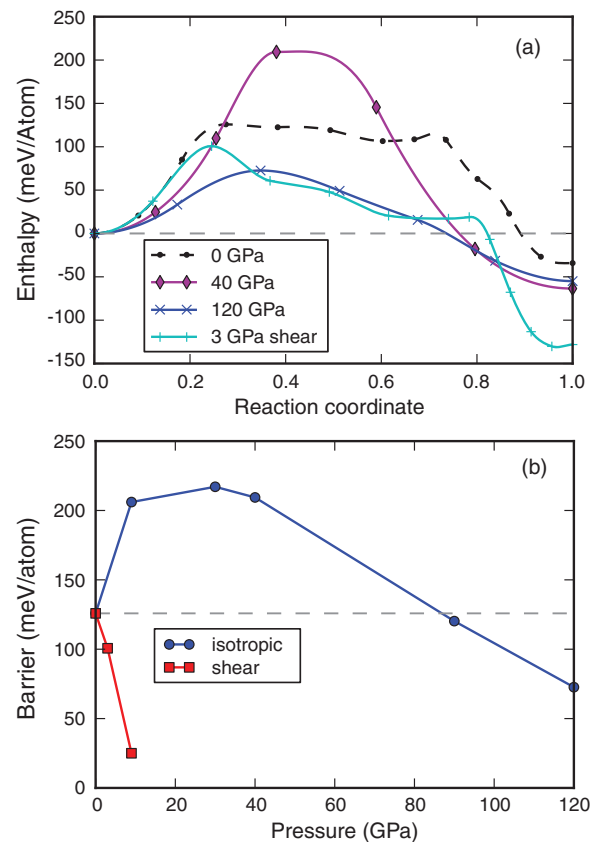


FIG. 3. (Color online) Comparison of different compression conditions: (a) MEPs under different pressures, with the energies of the Pv phases aligned to zero; (b) the enthalpy barriers as a function of pressure.

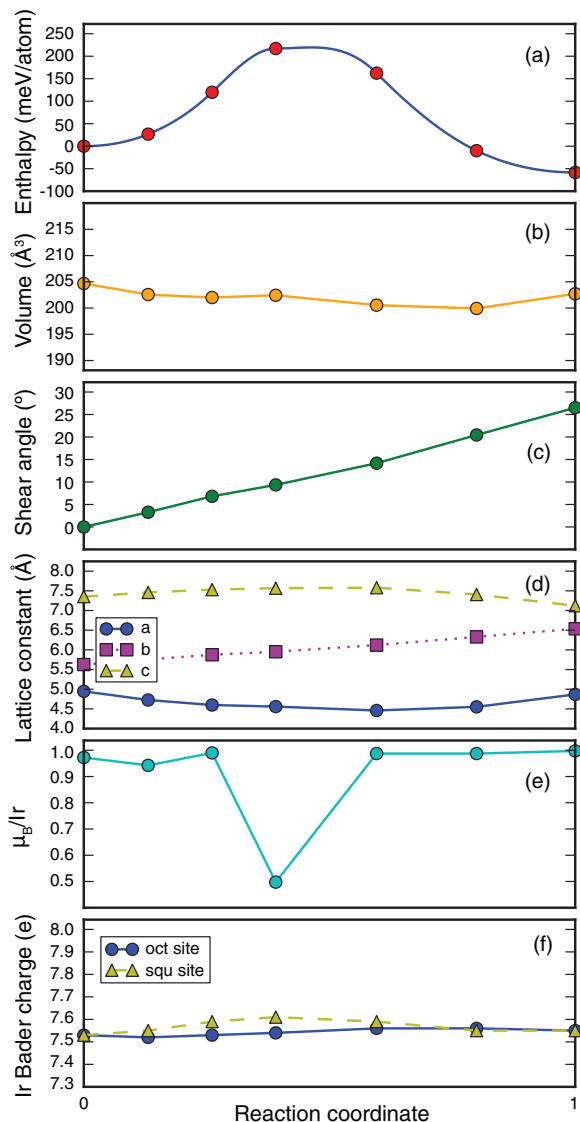


FIG. 4. (Color online) MEP at 30 GPa isotropic pressure and computed properties along the path.

the barrier whereas the isotropic pressure raises the barrier in the low-pressure regime below 20 GPa. The barrier change, however, is clearly nonlinear as the pressure increases and even drops after 30 GPa. After 90 GPa the isotropic pressure begins to lower the barrier compared to the zero pressure case. As shown in Fig. 3(a), the stabilization of the pPv product state due to isotropic pressure is significantly smaller than that due to shear stress. At 120 GPa the energies of the two phases are even closer than at 40 GPa because the Pv phase is more compressible and has a slightly smaller equilibrium volume at the high pressure. It is worth noticing that the intermediate minimum no longer exists in the isotropic pressure calculations.

A detailed analysis at 30 GPa is plotted in Fig. 4. The volume shrinks slightly at the saddle point while the shear deformation follows the same trend as under zero pressure. Taking the first-order approximation from this point, it is expected that increasing the isotropic or shear pressure will lower the barrier. The Bader analysis shows that under 30 GPa

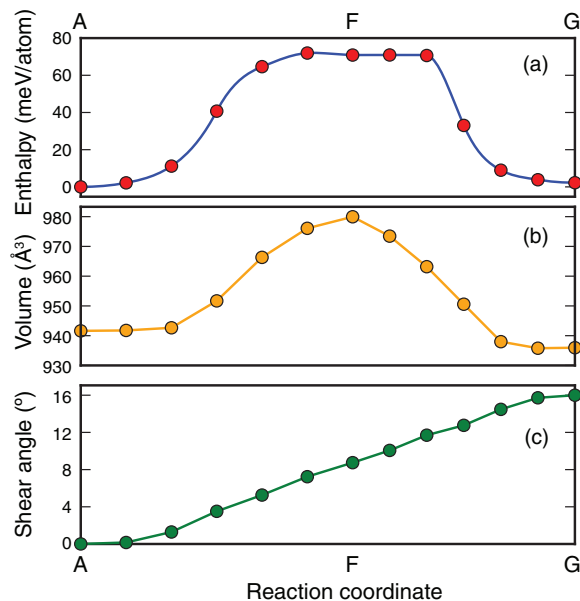


FIG. 5. (Color online) MEP of a larger supercell at zero pressure. The initial point (A) is the pure Pv phase; the intermediate (F) and final (G) states are shown in Fig. 6.

the charge transfer between the octahedral and square-planar sites are inhibited, resulting in a different spin moment transition along the path. As the pressure increases, the octahedral and square-planar sites tend to have similar local environment: becoming stretched octahedra but with different orientations.

So far we have considered only the concerted mechanism which is described by a small unit cell. To investigate the possibility of a more localized phase-transition mechanism, we enlarge the supercell size along the *a* and *b* directions. The zero pressure MEP calculations for this large cell are shown in Fig. 5. Instead of every other IrO_6 group rotating at the same time, now one layer transforms first and another layer follows, which agrees with the observation in Ref. 12. A laminate structure (G) is observed as a new intermediate minimum along the path, which is recognized as a mixture of the Pv and pPv phases rather than a new phase. The ratio of the two phases in the laminate is limited by the supercell size selected for the calculation; it does not reflect the actual situation expected in experiment. The critical nucleus size of the new phase would be interesting, but it is hard to estimate with DFT because of the large cell sizes necessary. Switching from the concerted to the nonconcerted mechanism,

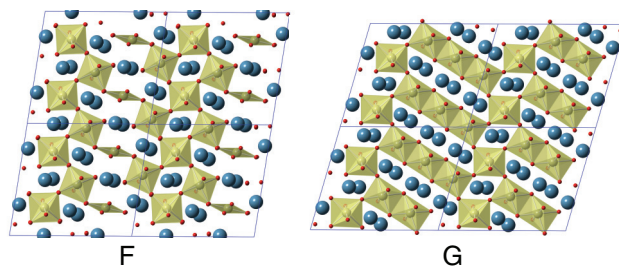


FIG. 6. (Color online) Structures of the intermediate (F) and final (G) minima of the larger supercell.

however, does not change the calculated trends of barrier as a function of pressure and shear stress. The nonconcerted mechanism introduces a phase boundary into the transition process, but the boundary does not change the volume or shear deformation direction along the path, as shown in Figs. 5(b) and 5(c).

III. DISCUSSION

The role of temperature in the phase transition is to provide the system with fluctuations to overcome the reaction barrier. A higher barrier requires a higher temperature for the transition to occur. An applied stress can change the enthalpy landscape and thus the barrier height, either an increase or a decrease. At a given external pressure, the barrier height between the two phases can be related to the onset temperature of the transition. For the Pv-to-pPv phase transition in CaIrO₃; the barrier height increases with the external isotropic pressure, therefore we predict the onset temperature of the transition will also increase. A suitable experiment for testing our calculated mechanism is as follows: under a given pressure (helium mediated), gradually increase the temperature of the Pv phase to find the temperature where the pPv phase is first observed. Repeat the process at different pressures and get a series of onset temperatures. One possible obstacle is that without any shear stress, the temperature required to activate the transition might be too high, at pressures below 30 GPa. A possible solution is to maintain a constant 9-GPa shear stress and vary the helium gas pressure, which can bring down the barrier to an observable region and allow the study of the unusual isotropic stress effect. Measuring the spin magnetic moment change during the phase transition is another possible way to verify the predicted mechanism.

The Pv-to-pPv phase transition is similar to the iron bcc-to-hcp transition. The shear effect and the microstructures we find here both agree qualitatively with the multiscale model results

in Ref. 28. In that work, the authors adopted the microstructure from experimental observations while we find the laminate directly from atomic simulations.

IV. CONCLUSION

In conclusion, we have provided a detailed mechanism of the Pv-to-pPv phase transition as a continuous path in the space of both atoms and lattice parameters. Based upon this path, we have shown how pressure and shear affect the reaction barrier. The shear stress lowers the barrier, while the isotropic pressure first raises the barrier and then lowers it with a crossover point of 90 GPa. These calculations explain the recent experimentally observed phase transformations under different compression conditions. Charge transfer between different iridium sites during the transition is predicted under low isotropic pressure or pure shear stress, which should be accompanied by a change in the spin magnetic moment. Bell's theory provides a straightforward understanding of the pressure effect from the transition path within small pressure deviation, but it may lead to completely opposite conclusion if the applied stress is far from the perturbation limit.

ACKNOWLEDGMENTS

This work is supported as part of the program "Understanding Charge Separation and Transfer at Interfaces in Energy Materials (EFRC:CST)," an Energy Frontier Research Center funded by the US Department of Energy, Office of Science, Office of Basic Energy Sciences under Award No. DE-SC0001091. J.S.Z. and J.B.G. were supported by the NSF MIRT program (DMR-1122603). Calculations were done with resources from the National Energy Research Scientific Computing Center and the Texas Advanced Computing Center. We thank L. Zhang for helpful discussions.

*henkelman@cm.utexas.edu

¹M. Murakami, K. Hirose, K. Kawamura, N. Sata, and Y. Ohishi, *Science* **304**, 855 (2004).
²A. R. Oganov and S. Ono, *Nature (London)* **430**, 445 (2004).
³T. Tsuchiya, J. Tsuchiya, K. Umemoto, and R. M. Wentzcovitch, *Earth Planet. Sci. Lett.* **224**, 241 (2004).
⁴H. Kojitani, Y. Shirako, and M. Akaogi, *Phys. Earth Planet. Inter.* **165**, 127 (2007).
⁵K. Niwa, T. Yagi, K. Ohgushi, S. Merkel, N. Miyajima, and T. Kikegawa, *Phys. Chem. Miner.* **34**, 679 (2007).
⁶S. Tateno, K. Hirose, N. Sata, and Y. Ohishi, *Phys. Earth Planet. Inter.* **181**, 54 (2010).
⁷K. Yamaura, Y. Shirako, H. Kojitani, M. Arai, D. P. Young, M. Akaogi, M. Nakashima, T. Katsumata, Y. Inaguma, and E. Takayama-Muromachi, *J. Am. Chem. Soc.* **131**, 2722 (2009).
⁸T. Tsuchiya and J. Tsuchiya, *Phys. Rev. B* **76**, 144119 (2007).
⁹J.-G. Cheng, J.-S. Zhou, and J. B. Goodenough, *Phys. Rev. B* **82**, 132103 (2010).
¹⁰K. Niwa, N. Miyajima, Y. Seto, K. Ohgushi, H. Gotou, and T. Yagi, *Phys. Earth Planet. Inter.* **194–195**, 10 (2012).

¹¹K. Niwa, T. Yagi, and K. Ohgushi, *Phys. Chem. Miner.* **38**, 21 (2010).
¹²A. R. Oganov, R. Martonák, A. Laio, P. Raiteri, and M. Parrinello, *Nature (London)* **438**, 1142 (2005).
¹³K. J. Caspersen and E. a. Carter, *Proc. Natl. Acad. Sci. USA* **102**, 6738 (2005).
¹⁴D. Sheppard, P. Xiao, W. Chemelewski, D. D. Johnson, and G. Henkelman, *J. Chem. Phys.* **136**, 074103 (2012).
¹⁵S. G. Mayr, *Phys. Rev. Lett.* **97**, 195501 (2006).
¹⁶S. S. M. Konda, J. N. Brantley, C. W. Bielawski, and D. E. Makarov, *J. Chem. Phys.* **135**, 164103 (2011).
¹⁷W. Kohn, A. D. Becke, and R. G. Parr, *J. Phys. Chem.* **100**, 12974 (1996).
¹⁸G. Kresse and J. Furthmüller, *Comput. Mater. Sci.* **6**, 15 (1996).
¹⁹G. Kresse and J. Furthmüller, *Phys. Rev. B* **54**, 11169 (1996).
²⁰J. P. Perdew, in *Electronic Structure of Solids*, edited by P. Ziesche and H. Eschrig (Akademie Verlag, Berlin, 1991), pp. 11–20.
²¹P. E. Blöchl, *Phys. Rev. B* **50**, 17953 (1994).
²²G. Kresse and D. Joubert, *Phys. Rev. B* **59**, 1758 (1999).
²³A. Subedi, *Phys. Rev. B* **85**, 020408 (2012).

²⁴See Supplemental Material at <http://link.aps.org/supplemental/10.1103/PhysRevB.88.144102> for movies of the reaction mechanisms.

²⁵R. F. W. Bader, *Atoms in Molecules: A Quantum Theory* (Oxford University Press, New York, 1990).

²⁶W. Tang, E. Sanville, and G. Henkelman, *J. Phys.: Condens. Matter* **21**, 084204 (2009).

²⁷G. Bell, *Science* **200**, 618 (1978).

²⁸K. J. Caspersen, A. Lew, M. Ortiz, and E. A. Carter, *Phys. Rev. Lett.* **93**, 115501 (2004).